Electronic Supplementary Information (ESI)

Core-Shell Nanoparticle with Tensile Strain Enables Highly Efficient Electrochemical Ethanol Oxidation

Moxuan Liu,[a#] Miao Xie,[b#] Yilan Jiang,[c] Zhaojun Liu,[a] Yiming Lu,[b] Shumeng Zhang,[a] Zhixue Zhang,[a] Xiaoxiao Wang,[a] Kai Liu,[a] Qing Zhang,[c] Tao Cheng,*[b] and Chuanbo Gao*[a]

[a] *Center for Materials Chemistry, Frontier Institute of Science and Technology, and State Key Laboratory of Multiphase Flow in Power Engineering, Xi'an Jiaotong University, Xi'an, Shaanxi 710054, China.*

[b] *Institute of Functional Nano & Soft Materials (FUNSOM), Jiangsu Key Laboratory for Carbon-Based Functional Materials & Devices, Joint International Research Laboratory of Carbon-Based Functional Materials and Devices, Soochow University, Suzhou, Jiangsu 215123, China.*

[c] *Center for High-resolution Electron Microscopy (ChEM), School of Physical Science and Technology, ShanghaiTech University, Shanghai 201210, China.*

[#] *M.L. and M.X. contributed equally to this work.*

Email: gaochuanbo@mail.xjtu.edu.cn (C.G.); tcheng@suda.edu.cn (T.C.)

Full Experimental Details

Materials. Silver nitrate ($AgNO_3$), sodium tetrachloropalladate (Na_2PdCl_4), palladium nitrate [$Pd(NO_3)_2$], glucose, diethylamine (DEA), sodium hydroxide (NaOH), polyvinylpyrrolidone (PVP) (Mw 40,000), PVP (Mw 55,000), sodium borohydride ($NaBH_4$), trisodium citrate dihydrate (TSC), hydrogen peroxide (H_2O_2, 30%), silver trifluoroacetate (CF_3COOAg), sodium hydrosulfide (NaSH), hydrochloric acid (HCl, 37%), ethylene glycol (EG), ethanol (C_2H_5OH), formaldehyde (HCHO), formic acid (HCOOH), acetaldehyde (CH_3CHO), acetic acid (CH_3COOH), glycerol, and potassium hydroxide (KOH) were purchased from Sigma-Aldrich. All chemicals were used as purchased without further purification.

Synthesis of Ag nanoplates. Ag nanoplates (edge length, ~35 nm) were synthesized by a modified thermal reduction method.[1] Typically, aqueous solutions of TSC (0.075 M, 24 mL), $AgNO_3$ (0.1 M, 400 μL), and H_2O_2 (30%, 960 μL) were added to 400 mL of H_2O in sequence. A fresh $NaBH_4$ solution (0.1 M, 2.4 mL) was then quickly injected into the above solution under vigorous stirring. After stirring at 25 °C for 30 min, the solution was collected and aged for 6 h. Finally, the Ag nanoplates were concentrated to a volume of 24 mL (Ag: ~1.7×10^{-3} M).

Synthesis of Ag@AgPd core-shell nanoplates. Typically, 64.5 mL of H_2O, 10 mL of PVP (Mw 40,000, 5 wt%), 1.5 mL of NaOH (0.5 M), 1.5 mL of DEA, 2 mL of glucose (0.5 M), 20 mL of Ag nanoplates (edge length: ~ 35 nm, Ag: ~1.7 mM), and 0.2–0.6 mL of $NaPdCl_4$ (0.05 M) were added to a glass vial in sequence under vigorous stirring at 60 °C. The glucose serves as the ligand and a reducing agent for the Pd (II) salt. After stirring for 6 h, Ag@AgPd core-shell nanoplates were collected by centrifugation, washed with H_2O, and redispersed in 2 mL of H_2O.

Synthesis of Ag-Pd alloy nanoparticles. Ag-Pd alloy nanoparticles were synthesized by following a previously reported protocol.[2] Typically, in a 50-mL round bottom flask, 14 mg of $Pd(NO_3)_2$, 6.5 mg (for $AgPd_{1.15}$, or 8.13 mg for $AgPd_{0.54}$) of $AgNO_3$, and 0.06 g of PVP (Mw 40, 000) were dissolved in 10 mL of EG under stirring. The mixture was heated at 160 °C for 2 h in an N_2 atmosphere. Ag-Pd alloy nanoparticles were collected by centrifugation, washed with acetone, and redispersed in 1 mL of H_2O.

Electrochemical measurements. All electrochemical measurements were taken on a CHI 760e workstation (CH Instruments, Inc.) with a three-electrode configuration at 25 °C. A rotating disk electrode (RDE, 0.196 cm^2), a Pt foil (1 cm × 1 cm), and a saturated calomel electrode (SCE) was used as the working, counter, and reference electrodes respectively. The Ag@AgPd core-shell nanoplates were supported on Vulcan XC-72 carbon and dispersed in H_2O/isopropanol/Nafion (5%) (1:1:0.004,

volume ratio) to form a stable ink. Then, an aliquot of the ink containing 1 μg of Pd was dropped and dried on an RDE. CV curves were collected in either N_2-saturated 1 M KOH to evaluate the electrochemical active surface area (ECSA) or in N_2-saturated 1 M KOH + 1 M EtOH to evaluate the EOR activity, both in the potential range of 0.135~1.235 V vs. RHE at a sweep rate of 50 mV s^{-1}. The ECSA was calculated according to the following equation:[3]

$$\text{ECSA} = Q_{\text{PdO}}/(0.405\ \text{mC cm}^{-2} \times m_{\text{Pd}})$$

Q_{PdO}: charges associated with the PdO reduction; m_{Pd}: the mass of Pd

The CO-stripping voltammetry was conducted in 1 M KOH. The electrolyte was first bubbled with CO for 30 min at 0.235 V vs. RHE. Then, the gas was changed to N_2 and bubbled for another 30 min. After that, CV cycles were obtained in the potential range of 0.135~1.235 V vs. RHE at a sweep rate of 20 mV s^{-1} for 2 cycles.

Analysis of the C1- and C2-path Faradaic efficiencies (FEs). The concentrations of the C2-path products, including CH_3COOH and CH_3CHO, were measured by HPLC. Standard curves were first obtained by plotting HPLC peak areas as a function of the concentrations. Typically, a series of solutions containing 0.1 M KOH, 1 M CH_3CH_2OH, and different concentrations of CH_3COOH were neutralized by excess H_2SO_4 and subjected to the HPLC analysis. A series of solutions containing 0.1 M KOH, 1 M CH_3CH_2OH, and different concentrations of CH_3CHO were prepared, derived with excess $NH_2OH{\cdot}HCl$, and subjected to the HPLC analysis. The standard curves are shown in **Fig. S1**. A chronoamperometric *i-t* test was conducted at 0.635 V vs. RHE in N_2-saturated 0.1 M KOH + 1 M EtOH for each catalyst. The *i-t* test was stopped when the quantity of electricity reached 50 C. The electrolyte was then sampled and analyzed by HPLC, with the concentrations of CH_3COOH and CH_3CHO calculated according to the standard curves. The FEs of the C2-path products can thus be calculated. Specifically, FE = mnF/Q, where F is the Faraday constant, m is the quantity of the product (mol), and n is the transferred electrons (n = 2 for CH_3CHO; n = 4 for CH_3COOH). The FE of the C1-path reaction to produce CO_2 was calculated by subtracting the C2-path FE from a 100% FE, assuming no side reactions. The FEs of the C1- and C2-path products with different catalysts are summarized in **Table S1**.

Estimation of the Pd-shell thickness: The estimation is based on a triangular Ag nanoplate (edge length, 35 nm; thickness, 5 nm), with basal {111} facets and side {100} facets for simplification. Then, the Pd/Ag ratio is calculated when 1, 2, 3, 4, 5, and 6 atomic layers of Pd are grown on the Ag nanoplates, under the assumption that the shell is composed of Pd and the Pd atoms are uniformly

deposited on the Ag surface with the lattice size following that of the Ag cores (d_{111} = 0.236 nm, d_{110} = 0.289 nm).

The number of Ag atoms in the Ag nanoplate can be calculated to be:

$$\frac{\frac{\sqrt{3}}{4}\times 35^2}{\frac{\sqrt{3}}{2}\times d_{110}^2}\times\frac{5}{d_{111}}=155323$$

After 1 atomic layer of Pd is grown on the 2 basal facets and 3 side facets of the Ag nanoplate, the number of the Pd atoms in each Ag nanoplate can be calculated to be:

$$2\times\frac{\frac{\sqrt{3}}{4}\times(35+2d_{110})^2}{\frac{\sqrt{3}}{2}\times d_{110}^2}+3\times\frac{35+2d_{110}}{d_{110}}\times(\frac{5}{d_{111}}+2)=23715$$

Thus, Pd/Ag = 23715/155323 = 0.153.

Similarly, the Pd/Ag ratios can be calculated to be 0.314, 0.485, 0.665, 0.855, and 1.054 when 2, 3, 4, 5, and 6 layers of Pd are grown on the Ag surface respectively. A linear relationship between the Pd/Ag ratio and the number of the atomic layers of Pd can be established (**Fig. S2**).

Based on the standard curve, the number of the atomic layers of Pd on Ag nanoplates could be calculated according to the Pd/Ag ratio obtained experimentally by ICP-MS. The results are summarized in **Table S2**.

Characterizations. Transmission electron microscopy (TEM), high-resolution TEM (HRTEM), and spherical-aberration-corrected HRTEM were performed on a Hitachi HT-7700, a JEM-F200-TEM, and a JEM-ARM300F (Grand), respectively. UV-vis spectra were obtained on an Ocean Optics HR2000+ES UV-vis-NIR spectrophotometer with a DH-2000-Bal light source. X-ray diffraction (XRD) patterns were recorded on a Rigaku SmartLab powder X-ray diffractometer equipped with Cu Kα radiation. X-ray photoelectron spectroscopy (XPS) was measured on an ESCALAB Xi+ with monochromatic Al Kα radiation. Inductively coupled plasma mass spectrometry (ICP-MS) was measured on a PerkinElmer NexION 350D. HPLC analysis was performed on an Agilent 1260 LC liquid chromatography.

DFT calculation. The quantum mechanics (QM) calculations were carried out using the VASP software, version 5.4.4.[4-7] We used the Perdew, Burke, and Ernzerhof (PBE) flavor[8] of density functional theory (DFT) with the post-stage DFT-D3 method to correct for London dispersion (van der Waals attraction) with Becke-Johnson damping.[9] The projector augmented wave (PAW) method was used to account for core-valence interactions.[10] The kinetic energy cutoff for plane wave

expansions was set to 400 eV, and reciprocal space was sampled by the Γ-centered Monkhorst-Pack scheme with a grid of 3 × 3 × 1. The vacuum layer is at least 15 Å above the surface. The convergence criteria are 1×10^{-5} eV energy differences for solving the electronic wave function. The Methfessel-Paxton smearing of second order with a width of 0.1 eV was applied. All geometries (atomic coordinates) were converged to within 3×10^{-2} eV $Å^{-1}$ for maximal components of forces.

Simulation Models. We carried out DFT simulations for 5 systems, including Ag/Pd 3:1, 1:1, 1:3 (cell parameters following those of Ag to mimic the core-shell structure), Pd, and Ag-Pd 1:1 alloy. For the Pd model, we simulated 3 layers 4×4 (111) surface with the bottom two layers fixed using a cell parameter of $a = b = 11.004$ Å, $c = 19.493$ Å, $\alpha = \beta = 90°$, $\gamma = 120°$.

To simulate Ag/Pd 3:1, we start from the Ag bulk phase primary cell and replace one Ag to Pd with the cell parameters of Ag. We then cut the (111) surface to construct 3 layers of 4×4 (111) with the bottom two layers fixed using a cell parameter of $a = b = 11.556$ Å, $c = 19.718$ Å, $\alpha = \beta = 90°$, $\gamma = 120°$, to simulate the catalytic interface

To simulate Ag/Pd 1:3, we start from the Ag bulk phase primary cell and replace three Pd atoms with Ag with the cell parameters of Ag. We then cut the (111) surface to construct 3 layers of 4×4 (111) with the bottom two layers fixed to simulate the catalytic interface.

To simulate Ag/Pd 1:1, we start from the Ag bulk phase primary cell and replace one vertex Ag and one center Ag to Pd, representing the lowest energy configuration among the possible structures we investigated. The cell parameters are the same as those of Ag. We then cut the (111) surface to construct 3 layers of 4×4 (111) with the bottom two layers fixed. This model is used to mimic the catalytic interface of the core-shell structure.

Ag-Pd 1:1 alloy: Based on the Ag/Pd 1:1 model, the cell of the Ag-Pd alloy is optimized, and the cell volume changes during the optimization process. Finally, the cell parameters of the Ag-Pd alloy model are $a = b = 12.829$ Å, $c = 20.313$ Å, $\alpha = \beta = 90°$, $\gamma = 115°$.

We considered the top site, bridge site, and two hollow sites (*hcp* and *f*cc) and reported the lowest one in the manuscript in the calculation of adsorption energies.

For Pd, *OH on the bridge site has the lowest binding energy. The binding energies of *CO on the *hcp* and *fcc* sites are very close, while the adsorption on the *hcp* site is slightly lower.

For Ag/Pd 3:1, *OH on the *f*cc site has the lowest binding energy, and *CO on the *hcp* site has the lowest binding energy.

For Ag/Pd 1:1, *OH on the *f*cc site has the lowest binding energy, and *CO on the *hcp* site has the lowest binding energy.

For Ag/Pd 1:3, *OH on the *hcp* site has the lowest binding energy, and *CO on the *hcp* site has the lowest binding energy.

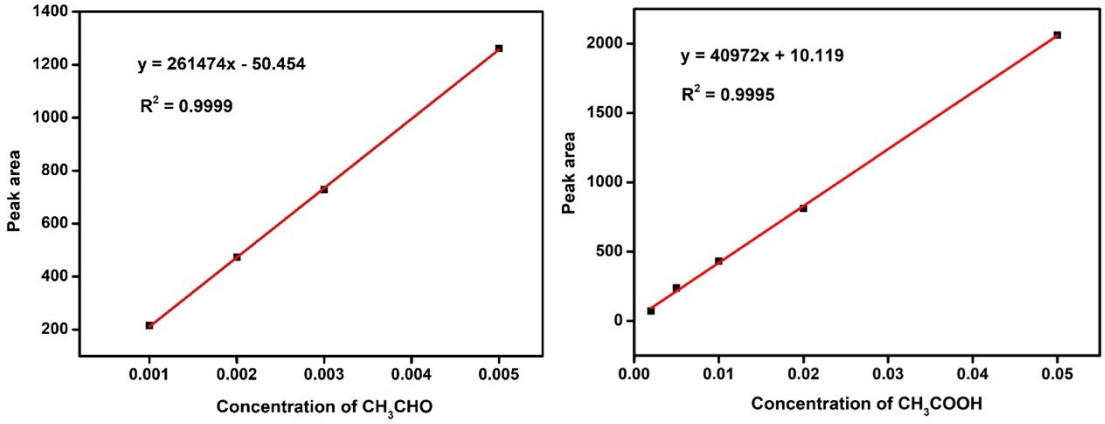

Fig. S1. Standard curves of CH_3CHO (left) and CH_3COOH (right).

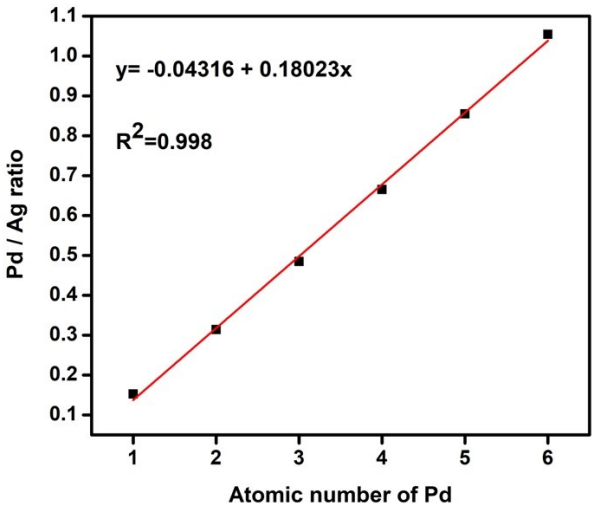

Fig. S2. Calculated linear relationship between the Pd/Ag ratio and the number of the atomic layers of Pd in a core-shell nanoplate.

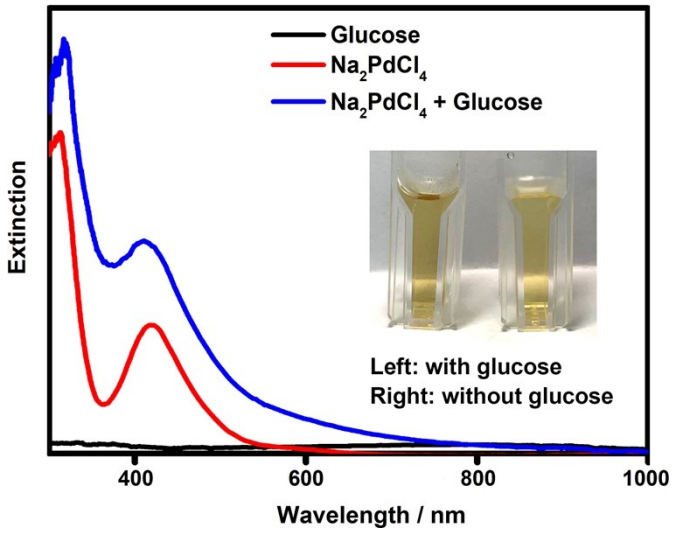

Fig. S3. UV-vis-NIR spectra of glucose, Na_2PdCl_4 solution, and a mixture of glucose and Na_2PdCl_4 after aging for 3 h at room temperature. Inset: Photographs of a Na_2PdCl_4 solution with and without the addition of glucose. The optical property evolution of the precursor solution can be explained by crystal field theory. The *d* orbitals of Pd split under the effect of the ligand field. When absorbing light, the electrons in the low-energy orbitals jump into higher-energy ones. The absorbed light energy corresponds to the splitting energy of the *d* orbitals. When Na_2PdCl_4 coordinates with glucose, the splitting energy changes significantly, which leads to variation in the light absorption and therefore a color change of the precursor.

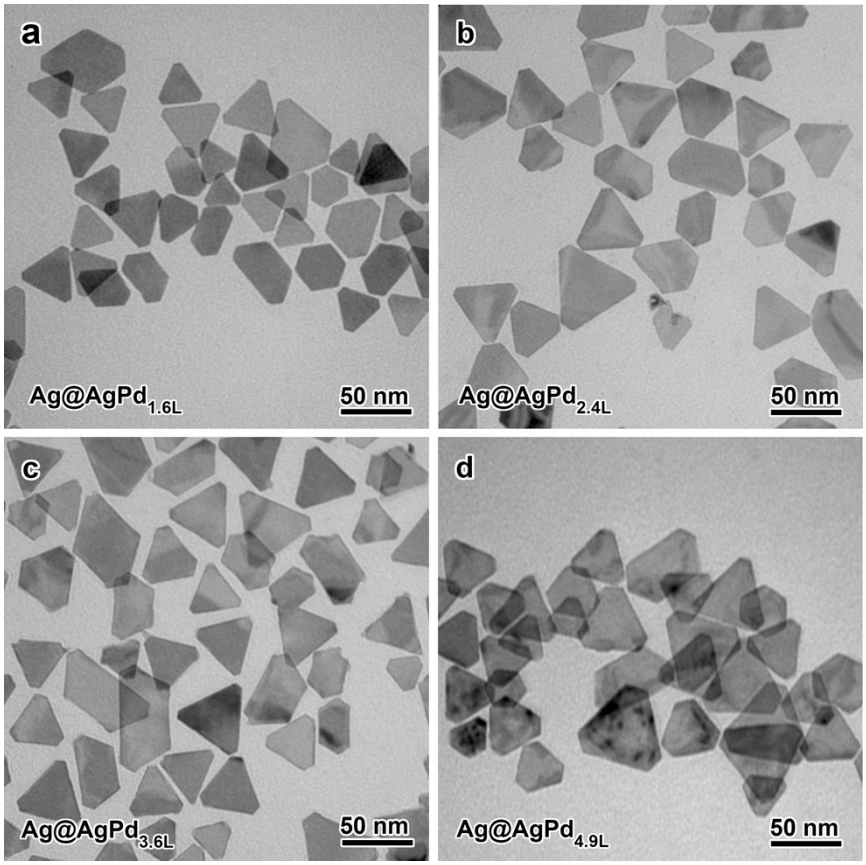

Fig. S4. TEM images of (a) Ag@AgPd$_{1.6L}$, (b) Ag@AgPd$_{2.4L}$, (c) Ag@AgPd$_{3.6L}$, and (d) Ag@AgPd$_{4.9L}$ core-shell nanoplates.

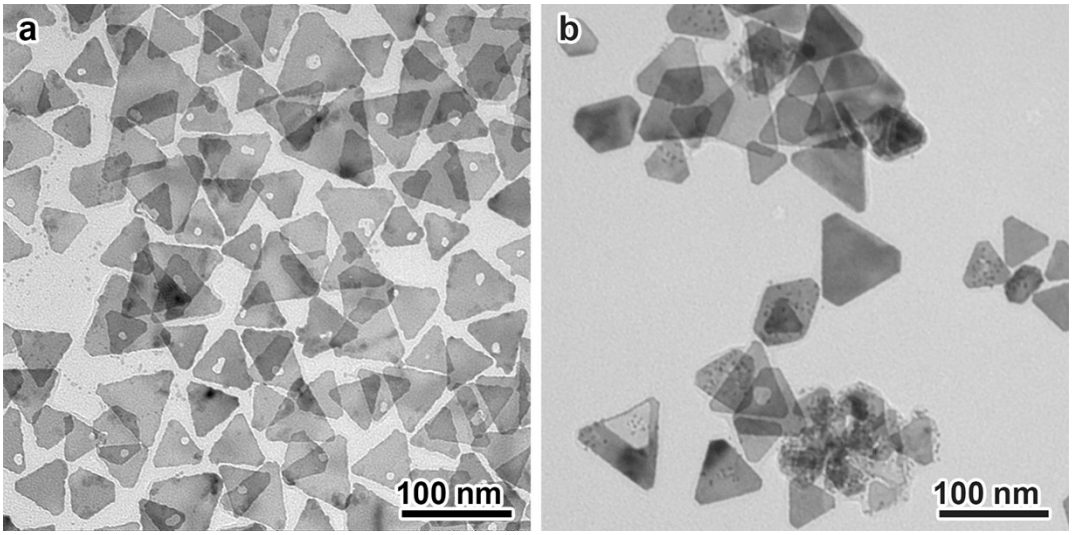

Fig. S5. TEM images of the Ag@AgPd core-shell nanoplates synthesized in the absence of (a) DEA or (b) glucose in a typical synthesis.

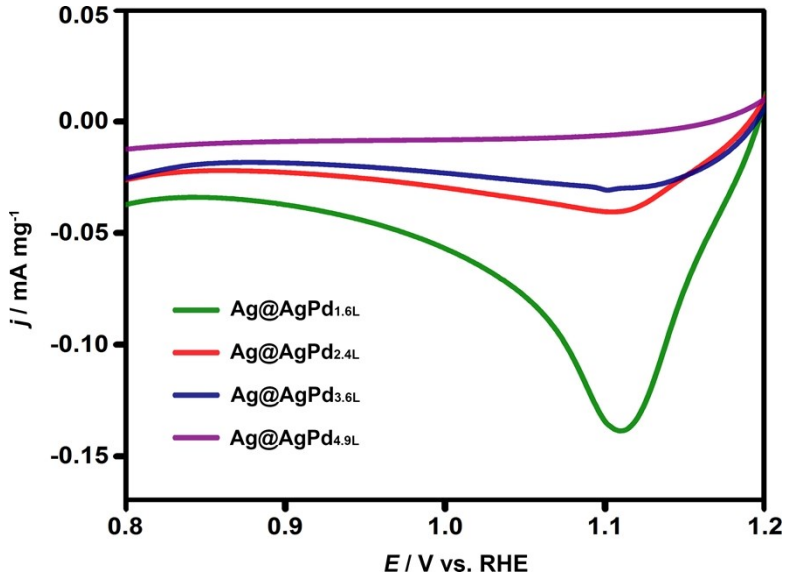

Fig. S6. CV curves of the Ag@AgPd core-shell nanoplates in N_2-saturated 1 M KOH, showing the reduction peaks of the surface Ag (I) at ~ 1.11 V vs. RHE. This peak is prominent when the coverage of Pd on the Ag nanoplates is still very low (Pd thickness, ~1.6 layers). Still, it decays dramatically and eventually undiscernible as the coverage of Pd increases (Pd thickness, ~2.4–4.9 layers), suggesting significantly reduced Ag-Pd alloying on the surface of the Ag@AgPd core-shell nanoplates with increasing thickness of the epitaxial layer.

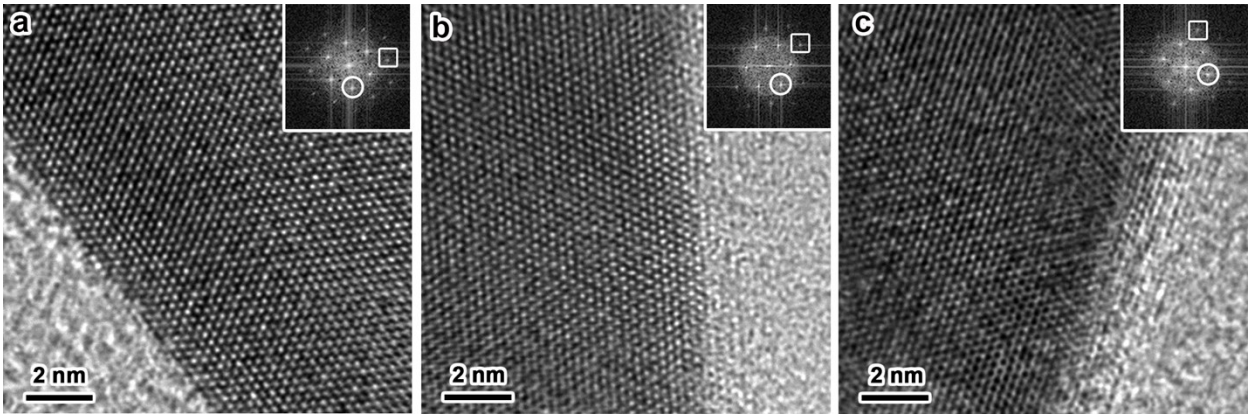

Fig. S7. HRTEM images of the Ag@AgPd core-shell nanoplates: a) Ag@AgPd$_{1.6L}$; b) Ag@AgPd$_{2.4L}$; c) Ag@AgPd$_{4.9L}$. Inset: Corresponding Fourier diffractogram patterns. The spots in squares and circles denote the {220} and ⅓{422} diffractions.

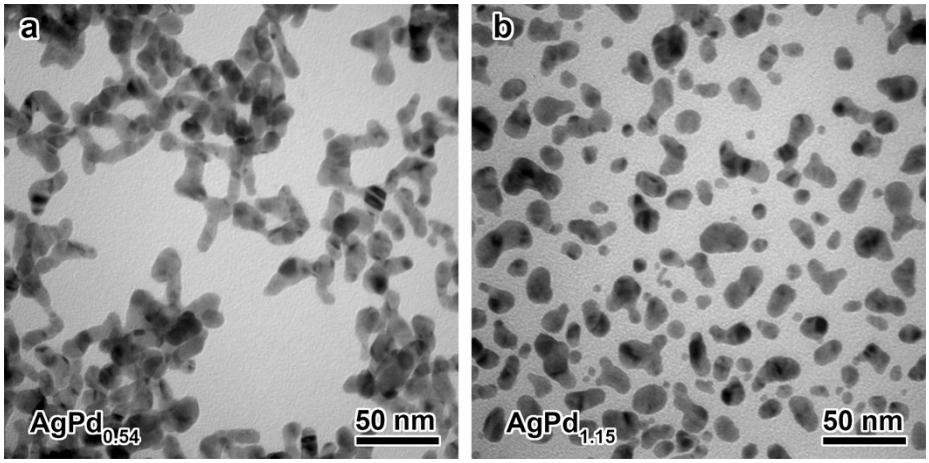

Fig. S8. TEM images of (a) $AgPd_{0.54}$ and (b) $AgPd_{1.15}$ alloy nanoparticles.

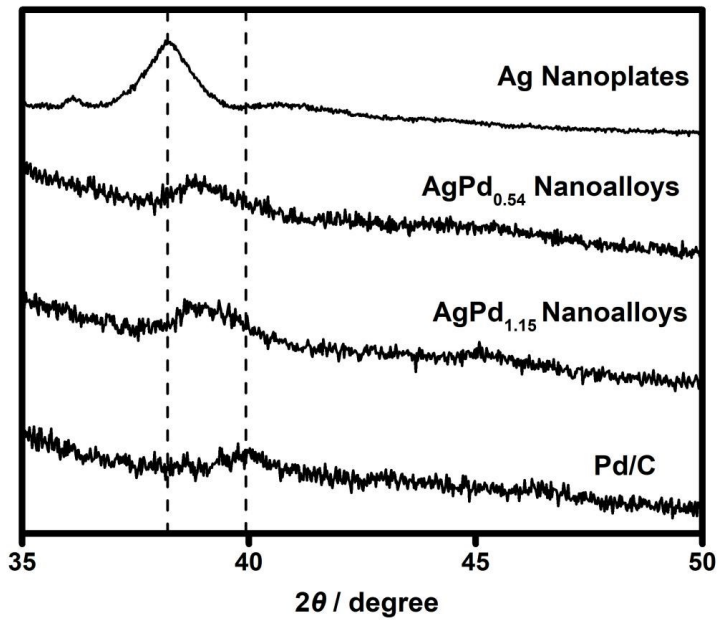

Fig. S9. XRD patterns of the $AgPd_{0.54}$ and $AgPd_{1.15}$ alloy nanoparticles in comparison with Ag nanoplates and the commercial Pd/C.

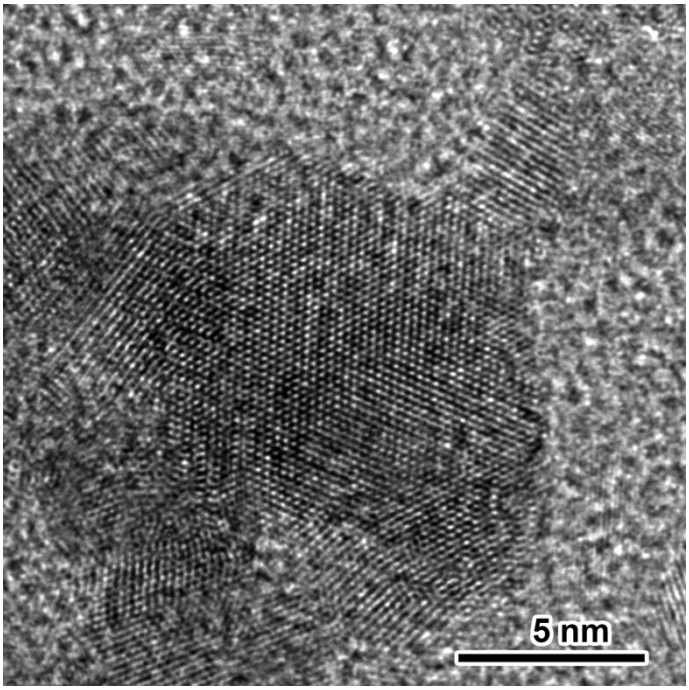

Fig. S10. HRTEM image of Ag-Pd alloy.

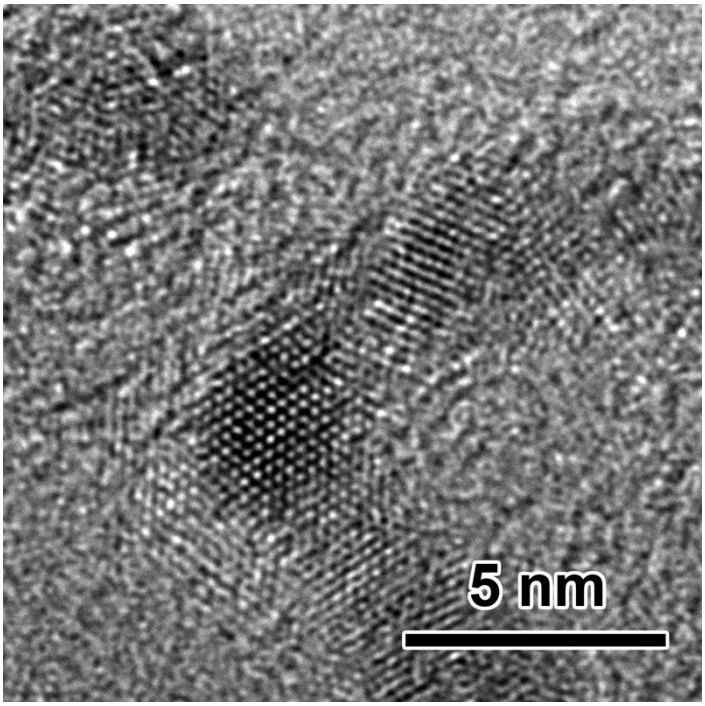

Fig. S11. HRTEM image of the commercial Pd/C.

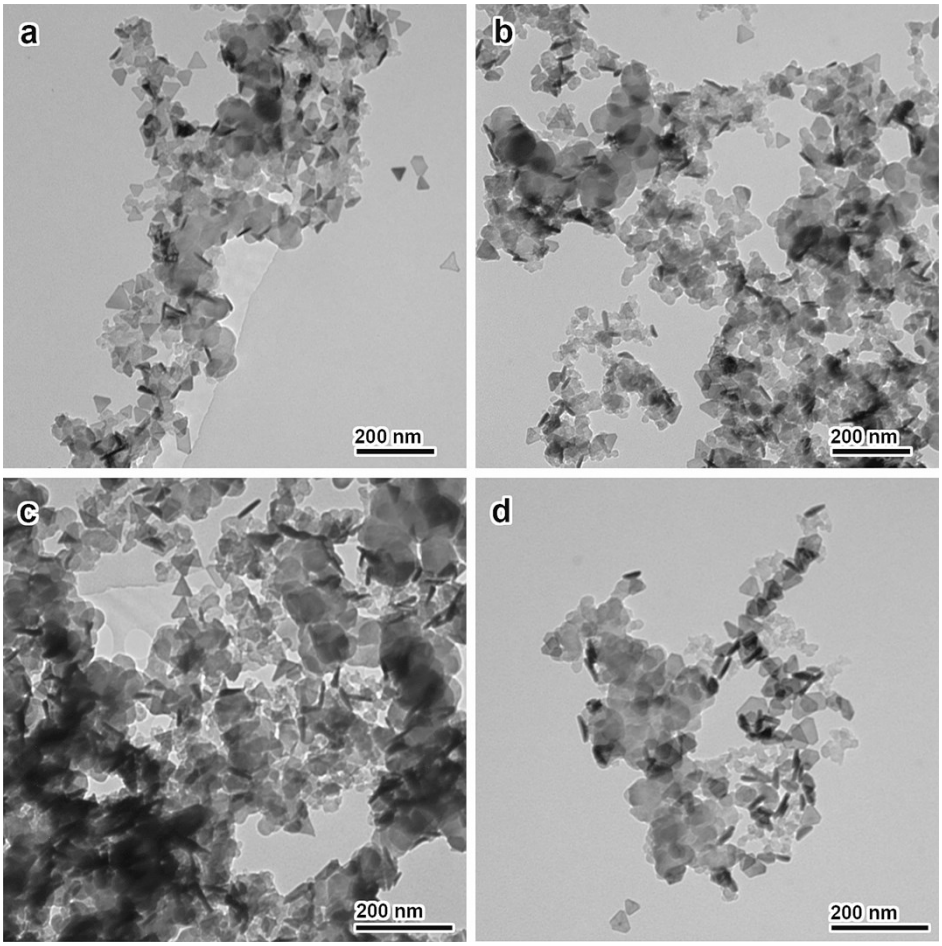

Fig. S12. TEM images of the carbon-supported Ag@AgPd core-shell nanoplates. (a) Ag@$AgPd_{1.6L}$; (b) Ag@$AgPd_{2.4L}$; (c) Ag@$AgPd_{3.6L}$; (d) Ag@$AgPd_{4.9L}$.

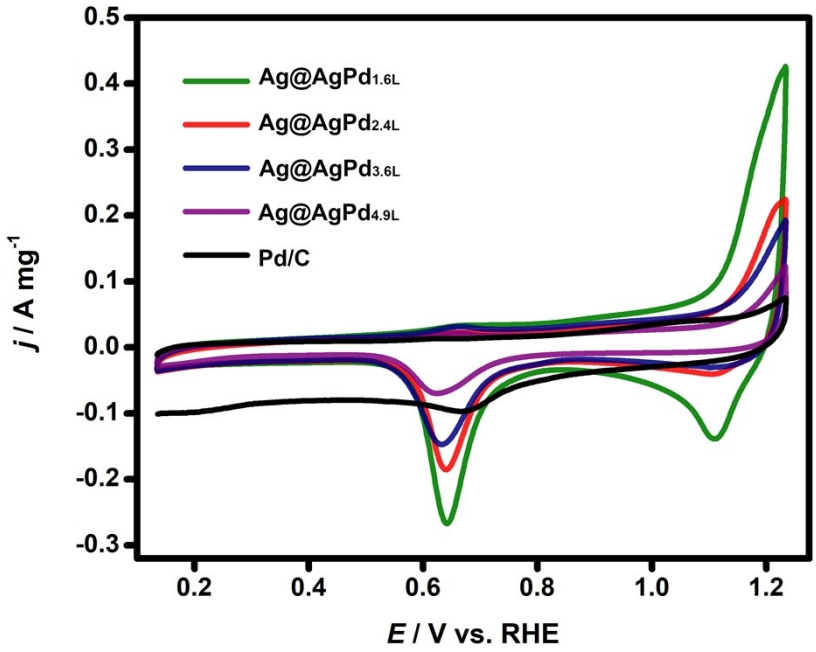

Fig. S13. CV curves of the Ag@AgPd core-shell nanoplates with different Pd-shell thickness compared with the commercial Pd/C, in N_2-saturated 1 M KOH at a scan rate of 50 mV s^{-1}.

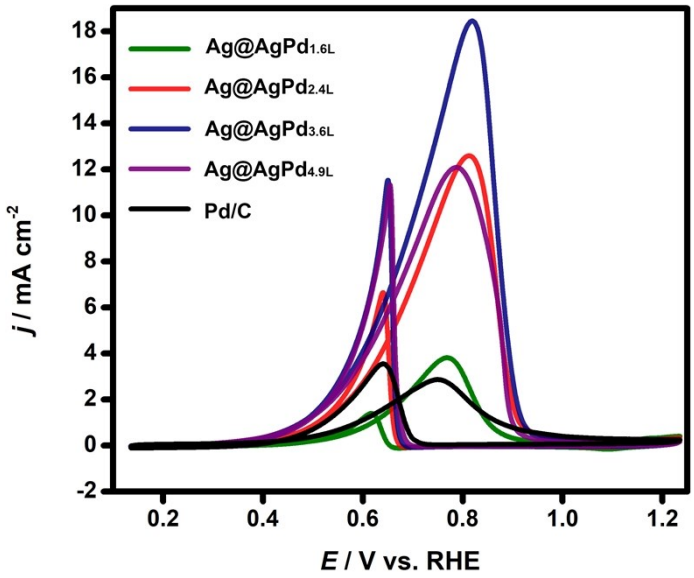

Fig. S14. CV curves (specific activities) of the Ag@AgPd core-shell nanoplates with different shell thickness compared with the commercial Pd/C in N_2-saturated 1 M KOH + 1 M ethanol at a scan rate of 50 mV s^{-1}.

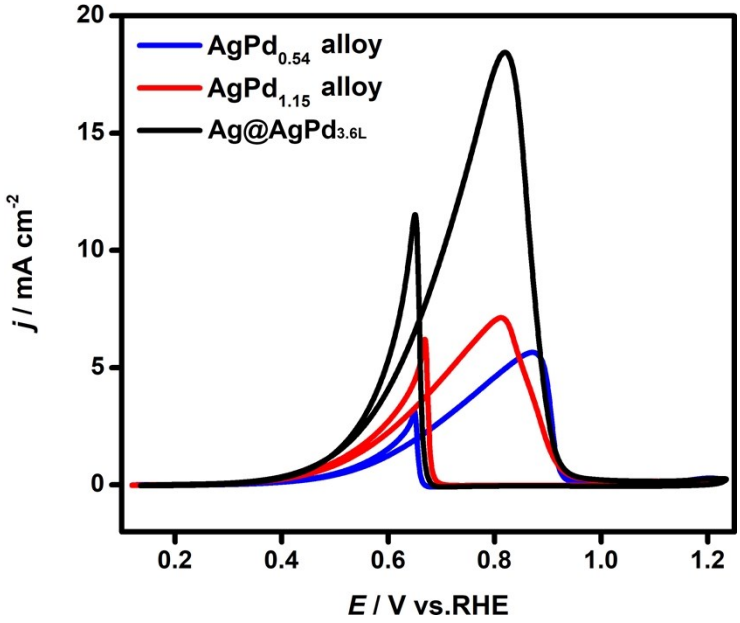

Fig. S15. CV curves (specific activities) of the Ag-Pd alloy nanoparticles and the Ag@AgPd core-shell nanoplates in N_2-saturated 1 M KOH + 1 M ethanol at a scan rate 50 mV s^{-1}.

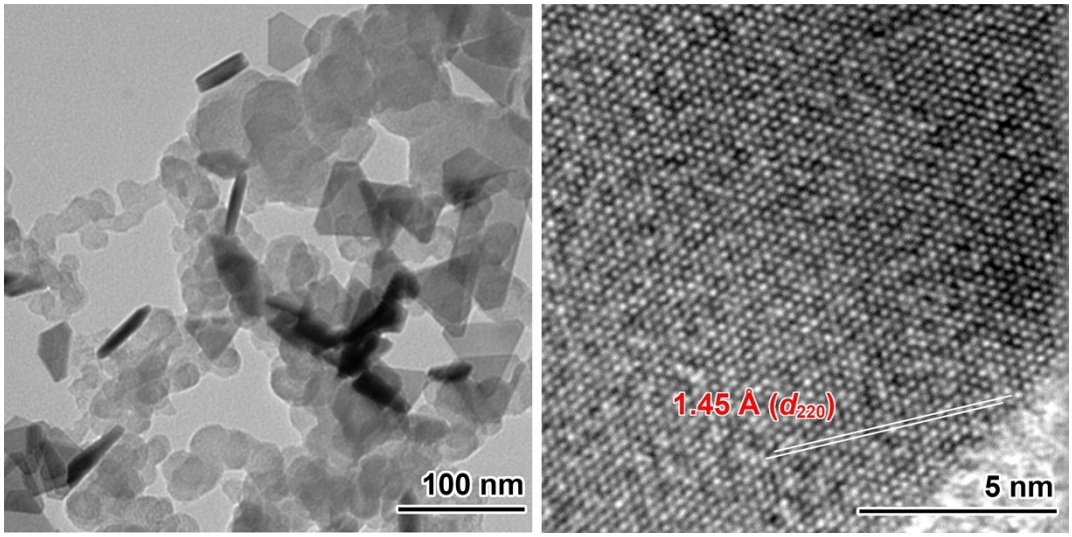

Fig. S16. TEM and HRTEM images of the Ag@$AgPd_{3.6L}$ nanoplates on carbon after the stability test.

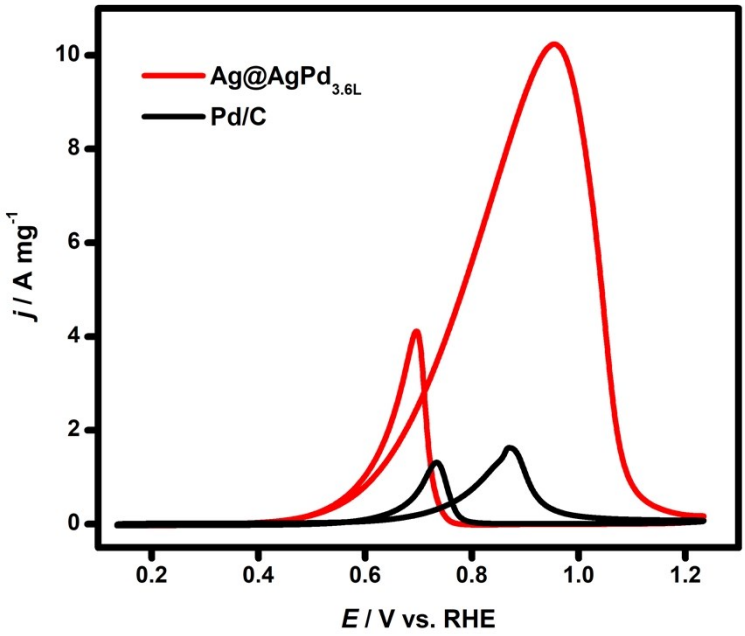

Fig. S17. Electrocatalytic ethylene glycol oxidation reaction (EGOR). CV curves of the Ag@AgPd$_{3.6L}$ core-shell nanoplates and the commercial Pd/C in N_2-saturated 0.5 M KOH + 0.5 M ethylene glycol at a scan rate 50 mV s^{-1}. The mass activities of the Ag@AgPd$_{3.6L}$ nanoplates and the Pd/C at the peak positions are 10.2 and 1.6 A mg^{-1}, respectively. The activity of the Ag@AgPd$_{3.6L}$ nanoplates in the electrocatalytic EGOR proves to be 6.3 times greater than that of the commercial Pd/C.

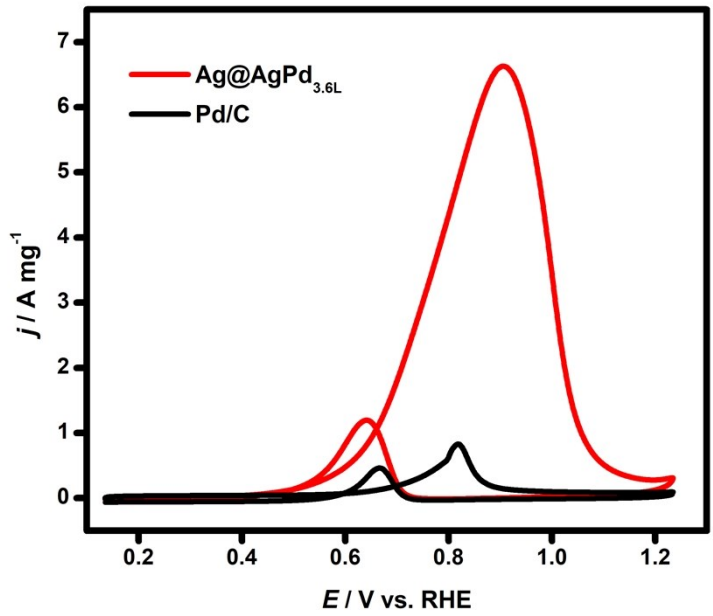

Fig. S18. Electrocatalytic glycerol oxidation reaction (GOR). CV curves of the $Ag@AgPd_{3.6L}$ core-shell nanoplates and the commercial Pd/C in N_2-saturated 1 M KOH + 0.1 M glycerol at a scan rate of 50 mV s^{-1}. The mass activities of the $Ag@AgPd_{3.6L}$ nanoplates and the Pd/C at the peak positions are 6.63 and 0.83 A mg^{-1}, respectively. The activity of the $Ag@AgPd_{3.6L}$ nanoplates in the electrocatalytic GOR proves to be 8.0 times greater than that of the commercial Pd/C.

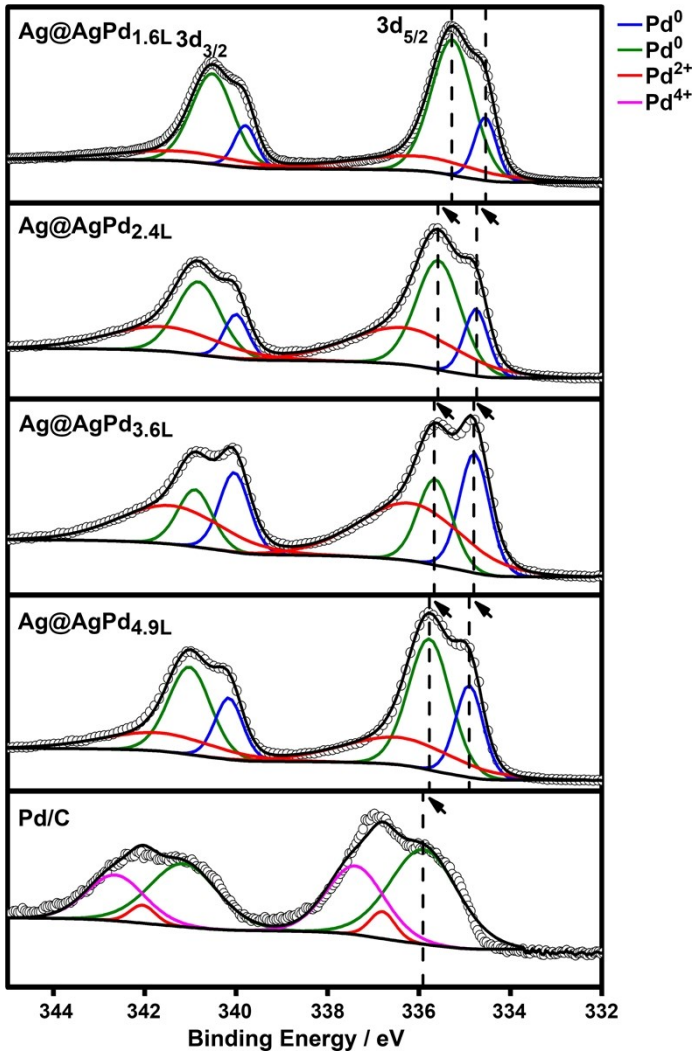

Fig. S19. Core-level Pd 3d XPS spectra of the Ag@AgPd$_{nL}$ core-shell nanoplates and the commercial Pd/C. The Pd 3d XPS spectra were fitted by the peaks of bulk Pd (0) (green lines), surfactant-capped surface Pd (0) (blue lines), Pd (II) (red lines), and Pd (IV) (purple lines). Pd (0) and Pd (II) exist in all Ag@AgPd$_{nL}$ core-shell nanoplates investigated, both showing a spectral shift to lower binding energies than those in the monometallic Pd/C. The shift in the binding energy becomes more prominent when the thickness of the Pd shells decreases. These observations confirm an efficient electron transfer from Ag to Pd sites.

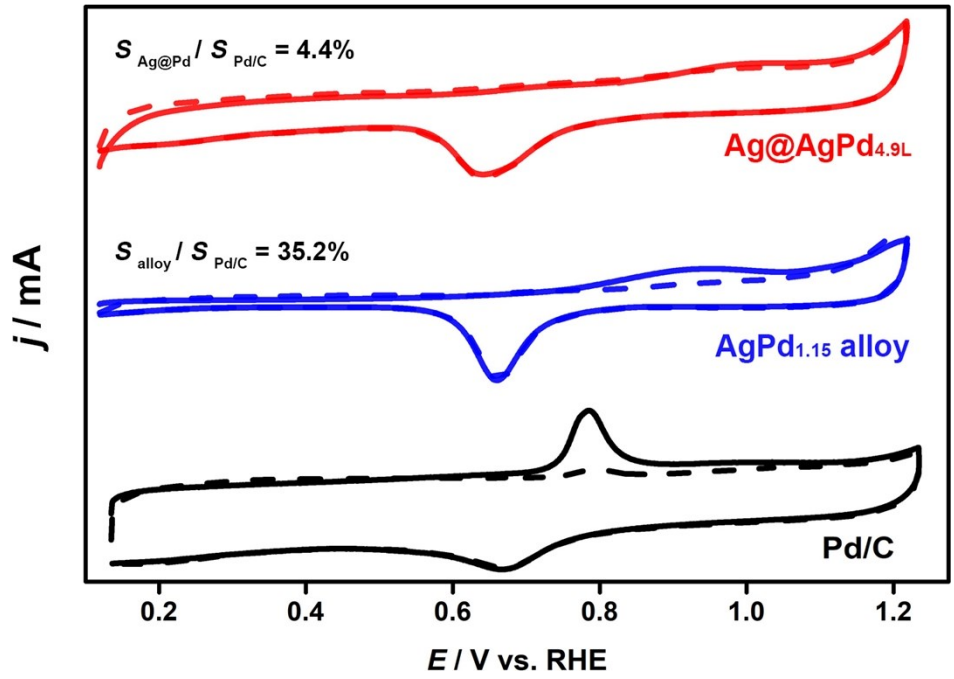

Fig. S20. CO stripping curves of the Ag@$AgPd_{4.9L}$ core-shell nanoplates, the $AgPd_{1.15}$ alloy nanoparticles, and the Pd/C in 1 M KOH at a scan rate 20 mV s^{-1}. All ECSAs of the nanoplates were normalized to that of the Pd/C. The solid and dashed lines indicate the first and second cycles of the scan, respectively.

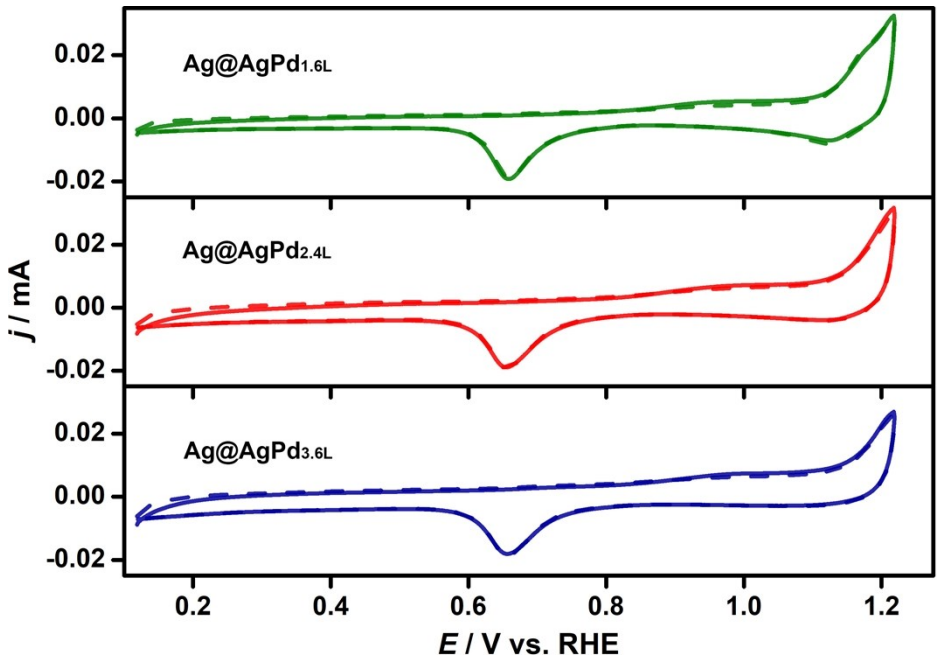

Fig. S21. CO stripping curves of the Ag@AgPd$_{n\mathrm{L}}$ core-shell nanoplates in 1 M KOH at a scan rate of 20 mV s^{-1}. All ECSAs of the nanoplates were normalized. The solid and dashed lines indicate the first and second cycles of the scan, respectively.

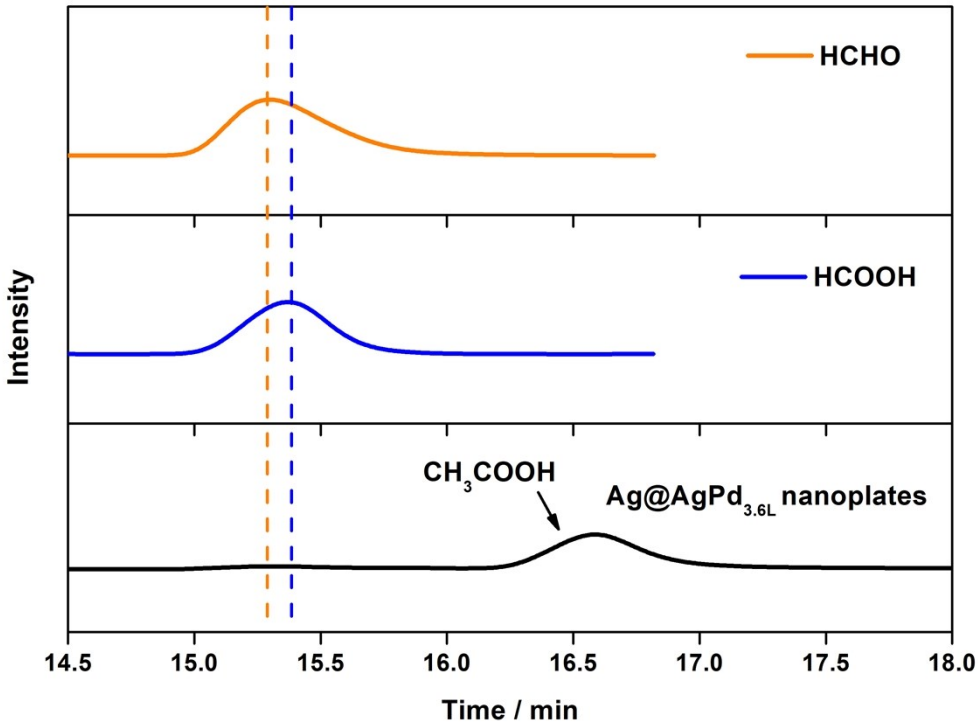

Fig. S22. HPLC analysis of the electrolyte after the quantity of electricity reached 50 C in an *i-t* test at 0.635 V *vs.* RHE. HPLC of pure HCHO and HCOOH in 0.1 M KOH are also listed for comparison. At the retention time of HCHO and HCOOH, no peaks are discernible in the HPLC profile of the EOR product, confirming the EOR under the conditions investigated does not afford the two species as the products.

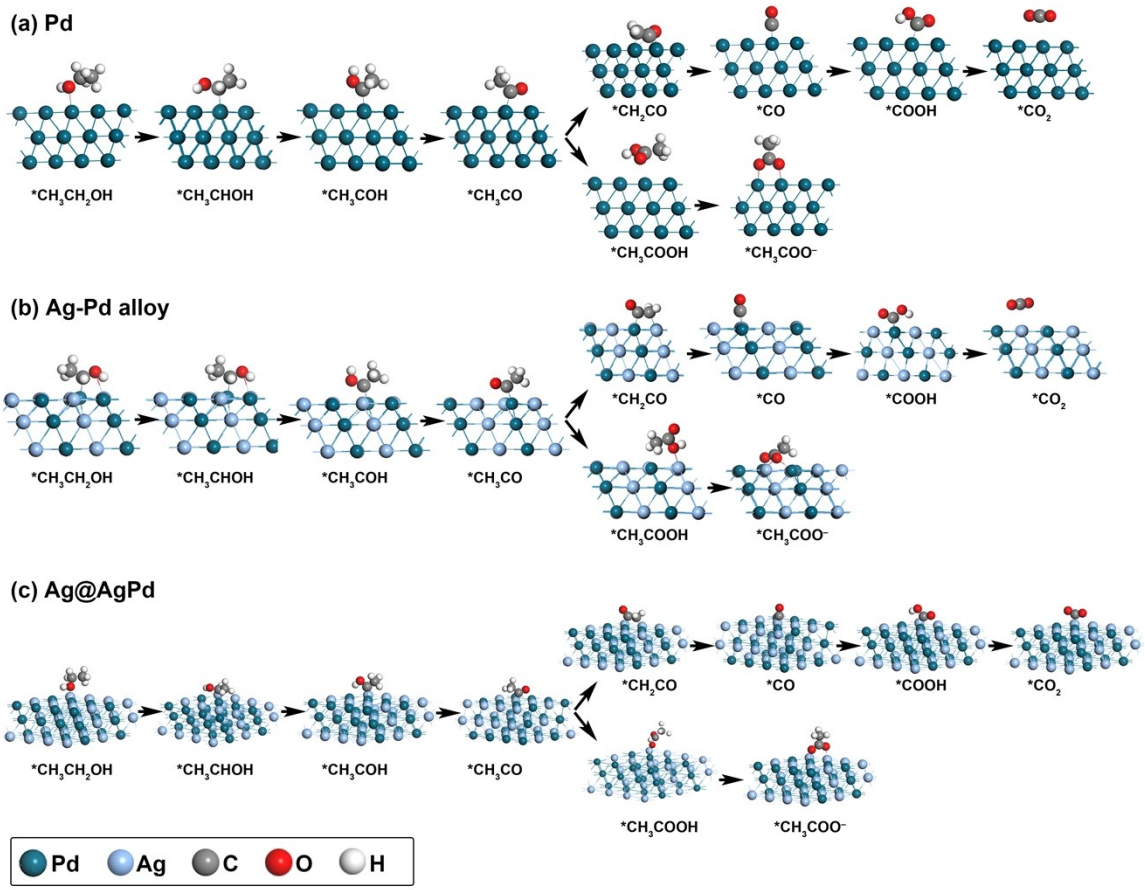

Fig. S23. Calculated configurations of the intermediates involved in the electrocatalytic EOR adsorbed on the surface of the catalysts: (a) Pd; (b) Ag-Pd alloy; (c)Ag@AgPd.

Table S1. Concentrations and Faradaic efficiencies of the C2- and C1-path products of the EOR with different catalysts.

Catalysts	CH_3COOH (mM)	CH_3CHO (mM)	Faradaic efficiency (C2 path)	Faradaic efficiency (C1 path)
$Ag@AgPd_{2.4L}$	0.283	0.291	82.69%	17.31%
$Ag@AgPd_{3.6L}$	0.28	0.29	82.01%	17.99%
$Ag@AgPd_{4.9L}$	0.303	0.291	86.55%	13.45%
$AgPd_{1.15}$ alloy	0.302	0.305	87.71%	12.29%
Pd/C	0.325	0.345	96.01%	3.99%

Table S2. Pd/Ag ratio in the Ag@AgPd core-shell nanoplates, measured by ICP-MS, and the calculated number of the atomic layers of Pd.

Pd/Ag ratio (by ICP-MS)	Number of Pd atomic layers (by calculation)
0.24	1.6
0.39	2.4
0.61	3.6
0.84	4.9

Table S3. Reproducibility of the electrocatalytic activities, showing the specific and mass activities of the catalysts measured from three parallel samples.

Catalysts	Specific activities / mA cm^{-2}		Mass activities / A mg^{-1}	
$Ag@AgPd_{1.6L}$	3.81	3.84 ± 0.06	3.07	3.09 ± 0.05
	3.93		3.16	
	3.78		3.04	
$Ag@AgPd_{2.4L}$	12.58	12.26 ± 0.35	9.13	8.90 ± 0.26
	11.77		8.54	
	12.44		9.02	
$Ag@AgPd_{3.6L}$	17.86	18.15 ± 0.23	12.50	12.71 ± 0.16
	18.17		12.72	
	18.43		12.90	
$Ag@AgPd_{4.9L}$	12.08	12.26 ± 0.34	4.40	4.47 ± 0.12
	12.73		4.64	
	11.96		4.36	
Ag-Pd alloy	7.12	7.27 ± 0.14	0.92	0.94 ± 0.02
	7.46		0.96	
	7.23		0.93	
Pd/C	2.81	2.79 ± 0.06	0.99	0.99 ± 0.02
	2.86		1.01	
	2.72		0.96	

Table S4. A literature survey showing the typical mass and specific activities of the EOR electrocatalysts in alkaline electrolytes.

Electrocatalyst	Electrolyte	Mass Activity ($A\ mg^{-1}$)	Specific Activity ($mA\ cm^{-2}$)	Publication Year	Reference
Ag@AgPd	**1.0 M KOH + 1.0 M EtOH**	**12.7**	**18.2**	–	**This work**
9 nm-$\mathbf{Pd_{61}Pt_{22}}Cu_{17}$ Nanorings	1.0 M KOH + 1.0 M EtOH	12.42	13.25	2020	11
Pd/a-$SrRuO_3$	1.0 M KOH + 1.0 M EtOH	4.0	–	2020	12
PdFe Nanocages	1.0 M KOH + 1.0 M EtOH	2.65	8.3	2020	13
PdCu-SnO_2 NWs	1.0 M KOH + 1.0 M EtOH	7.77	–	2020	14
Pd NW@cCuOx	1.0 M KOH + 1.0 M EtOH	0.63	7.19	2020	15
PdZn NSs	1.0 M NaOH + 1.0 M EtOH	2.73	–	2019	16
Pd-(SnO_2@C)/C	1.0 M KOH + 1.0 M EtOH	3.62	9.84	2019	17
$\mathbf{Pd_{31}}Cu_6Co_8$ NWs	1.0 M KOH + 1.0 M EtOH	7.45	8.01	2019	18
W@**Pd**/C	1.0 M NaOH + 1.0 M EtOH	9.54	–	2019	19
Au/THH **Pd** NCs	1.0 M NaOH + 0.5 M EtOH	–	12.7	2019	20
Au@**Pt**/C	1.0 M KOH + 1.0 M EtOH	6.9	–	2019	21
Au@**Pt**Ir/C	1.0 M KOH + 1.0 M EtOH	58*	–	2019	21
SANi–**Pt**NWs	1.0 M KOH + 1.0 M EtOH	5.60	–	2019	22
Au@**Pd**AuCu MNSs	1.0 M KOH + 1.0 M EtOH	3.99	–	2019	23
PdAg NWs	1.0 M KOH + 1.0 M EtOH	2.84	–	2019	24
PdAgCu MNSs	1.0 M KOH + 1.0 M EtOH	4.64	–	2019	25
Pd/Ag–BP	1.0 M NaOH + 1.0 M EtOH	6.0	–	2019	26

$Bi(OH)_3$/**Pd**Bi	1.0 M NaOH + 1.0 M EtOH	5.3	–	2019	27
PdAg NDs	1.0 M KOH + 1.0 M EtOH	2.63	3.7	2018	28
PtRhCu CNBs	1.0 M KOH + 1.0 M EtOH	4.09	14.9	2018	29
PtRhNi–ANAs	1.0 M KOH + 1.0 M EtOH	1.39	7.97	2017	30
$\mathbf{Pd}_4Au_1$–P/CNT	1.0 M KOH + 1.0 M EtOH	2.29	–	2017	31
4H/fcc Au@**Pd** NRs	1.0 M KOH + 1.0 M EtOH	2.92	–	2017	32
PdAg/rGO	1.0 M KOH + 1.0 M EtOH	3.13	1.2	2017	33
Pd/$Ni(OH)_2$/rGO	1.0 M KOH + 1.0 M EtOH	1.54	4.1	2017	3
PdNi-P	1.0 M NaOH + 1.0 M EtOH	4.95	–	2017	34
PdNi-HNCs-R/C	1.0 M KOH + 1.0 M EtOH	1.2	4.12	2017	35
PdCu NWs	1.0 M KOH + 1.0 M EtOH	3.47	–	2016	36
PdNi HNS	1.0 M NaOH + 1.0 M EtOH	3.63	6.54	2015	37
PdAu NWs	1.0 M KOH + 1.0 M EtOH	10.8	–	2014	38

***Note:** It can be inferred that the catalytic activity of the Ag@AgPd core-shell nanoplates substantially exceeds those of previously reported **Pd**-based catalysts. A higher mass activity was achieved with a **Pt**-based catalyst (Ref. 21).

Table S5. The comparison of Pd/Ag ratio in the $Ag@AgPd_{3.6L}$ core-shell nanoplates before and after stability test, measured by ICP-MS.

Catalyst	Pd/Ag ratio (by ICP-MS)
$Ag@AgPd_{3.6L}$-before stability test	0.603
$Ag@AgPd_{3.6L}$-after stability test	0.605

Table S6. A literature survey showing the typical mass activities of the EGOR electrocatalysts in alkaline electrolytes.

Electrocatalysts	Reaction Medium	Mass Activity ($A\ mg^{-1}$)	Reference
Ag@AgPd nanoplates	**0.5 M KOH + 0.5 M EG**	**10.20**	**This work**
PdAg nanoparticles	1.0 M KOH + 1.0 M EG	5.33	39
PdCu nanosheets	1.0 M KOH + 1.0 M EG	4.71	40
Ultrathin **PtPd**Ni nanosheets	0.5 M KOH + 0.5 M EG	11	41
Au-island-covered **Pd** nanotubes	0.5 M KOH + 0.5 M EG	7.53	42
PdAuNi nanosponges	0.5 M KOH + 0.5 M EG	6.36	43
Bimetallic **PdPt** nanowires	0.5 M KOH + 0.5 M EG	3.38	44

Table S7. A literature survey showing the typical mass activities of the GOR electrocatalysts in alkaline electrolytes.

Electrocatalysts	Reaction Medium	Mass Activity ($A\ mg^{-1}$)	Reference
Ag@AgPd nanoplates	**1 M KOH + 0.1 M glycerol**	**6.63**	**This work**
Ultrathin **PtPd**Ni nanosheets	1 M KOH + 0.1 M glycerol	6	41
Cu**PdPt** ultrathin nanowire networks	1 M KOH + 0.1 M glycerol	2.16	45
PdAuNi nanosponges	1 M KOH + 0.1 M glycerol	3.3	43
Au-island-covered **Pd** nanotubes	1 M KOH + 0.1 M glycerol	3.0	42
Bimetallic **PdPt** nanowires	1 M KOH + 0.1 M glycerol	1.8	44
$\mathbf{Pd}_x$Bi	1 M KOH + 0.1 M glycerol	0.8	46

References

1. G. S. Métraux and C. A. Mirkin, *Adv. Mater.*, 2005, **17**, 412-415.
2. K. Tedsree, T. Li, S. Jones, C. W. A. Chan, K. M. K. Yu, P. A. J. Bagot, E. A. Marquis, G. D. W. Smith and S. C. E. Tsang, *Nat. Nanotechnol.*, 2011, **6**, 302-307.
3. W. Huang, X. Y. Ma, H. Wang, R. Feng, J. Zhou, P. N. Duchesne, P. Zhang, F. Chen, N. Han, F. Zhao, J. Zhou, W. B. Cai and Y. Li, *Adv. Mater.*, 2017, **29**, 1703057.
4. G. Kresse and J. Hafner, *Phys. Rev. B: Condens. Matter Mater. Phys.*, 1993, **47**, 558-561.
5. G. Kresse and J. Furthmüller, *Comput. Mater. Sci.*, 1996, **6**, 15-50.
6. G. Kresse and J. Furthmüller, *Phys. Rev. B: Condens. Matter Mater. Phys.*, 1996, **54**, 11169-11186.
7. G. Kresse and J. Hafner, *Phys. Rev. B: Condens. Matter Mater. Phys.*, 1993, **47**, 558-561.
8. J. P. Perdew, K. Burke and M. Ernzerhof, *Phys. Rev. Lett.*, 1996, **77**, 3865-3868.
9. S. Grimme, J. Antony, S. Ehrlich and H. Krieg, *J. Chem. Phys.*, 2010, **132**, 154104.
10. G. Kresse and D. Joubert, *Phys. Rev. B: Condens. Matter Mater. Phys.*, 1999, **59**, 1758-1775.
11. W. Wang, X. Zhang, Y. Zhang, X. Chen, J. Ye, J. Chen, Z. Lyu, X. Chen, Q. Kuang, S. Xie and Z. Xie, *Nano Lett.*, 2020, **20**, 5458-5464.
12. X. Wu, J. He, M. Zhang, Z. Liu, S. Zhang, Y. Zhao, T. Li, F. Zhang, Z. Peng, N. Cheng, J. Zhang, X. Wen, Y. Xie, H. Tian, L. Cao, L. Bi, Y. Du, H. Zhang, J. Cheng, X. An, Y. Lei, H. Shen, J. Gan, X. Zu, S. Li and L. Qiao, *Nano Energy*, 2020, **67**, 104247.
13. H. Xu, H. Shang, C. Wang, L. Jin, C. Chen and Y. Du, *Nanoscale*, 2020, **12**, 2126-2132.
14. T. Song, F. Gao, L. Jin, Y. Zhang, C. Wang, S. Li, C. Chen and Y. Du, *J. Colloid Interface Sci.*, 2020, **560**, 802-810.
15. Z. Chen, Y. Liu, C. Liu, J. Zhang, Y. Chen, W. Hu and Y. Deng, *Small*, 2020, **16**, 1904964.
16. Q. Yun, Q. Lu, C. Li, B. Chen, Q. Zhang, Q. He, Z. Hu, Z. Zhang, Y. Ge, N. Yang, J. Ge, Y.-B. He, L. Gu and H. Zhang, *ACS Nano*, 2019, **13**, 14329-14336.
17. T. Qu, Q. Tan, Y. Chen, L. Liu, S. Guo, Y. Chen, Y. Liu, S. Li and Y. Liu, *ACS Appl. Energy Mater.*, 2019, **2**, 8449-8458.
18. F. Zhao, C. Li, Q. Yuan, F. Yang, B. Luo, Z. Xie, X. Yang, Z. Zhou and X. Wang, *Nanoscale*, 2019, **11**, 19448-19454.
19. Y. Yang, M. Tian, Q. Li, Y. Min, Q. Xu and S. Chen, *ACS Appl. Mater. Interfaces*, 2019, **11**, 30968-30976.
20. J. Guo, R. Huang, Y. Li, Z. Yu, L. Wan, L. Huang, B. Xu, J. Ye and S. Sun, *J. Phys. Chem. C*, 2019, **123**, 23554-23562.
21. Z. Liang, L. Song, S. Deng, Y. Zhu, E. Stavitski, R. R. Adzic, J. Chen and J. X. Wang, *J. Am. Chem. Soc.*, 2019, **141**, 9629-9636.
22. M. Li, K. Duanmu, C. Wan, T. Cheng, L. Zhang, S. Dai, W. Chen, Z. Zhao, P. Li, H. Fei, Y. Zhu, R. Yu, J. Luo, K. Zang, Z. Lin, M. Ding, J. Huang, H. Sun, J. Guo, X. Pan, W. A. Goddard, P. Sautet, Y. Huang and X. Duan, *Nat. Catal.*, 2019, **2**, 495-503.
23. H. Lv, L. Sun, X. Chen, D. Xu and B. Liu, *Green Chem.*, 2019, **21**, 2043-2051.
24. H. Lv, Y. Wang, A. Lopes, D. Xu and B. Liu, *Appl. Catal., B*, 2019, **249**, 116-125.

25. H. Lv, L. Sun, L. Zou, D. Xu, H. Yao and B. Liu, *Chem. Sci.*, 2019, **10**, 1986-1993.
26. T. Wu, Y. Ma, Z. Qu, J. Fan, Q. Li, P. Shi, Q. Xu and Y. Min, *ACS Appl. Mater. Interfaces*, 2019, **11**, 5136-5145.
27. X. Yuan, Y. Zhang, M. Cao, T. Zhou, X. Jiang, J. Chen, F. Lyu, Y. Xu, J. Luo, Q. Zhang and Y. Yin, *Nano Lett.*, 2019, **19**, 4752-4759.
28. W. Huang, X. Kang, C. Xu, J. Zhou, J. Deng, Y. Li and S. Cheng, *Adv. Mater.*, 2018, **30**, 1706962.
29. S.-H. Han, H.-M. Liu, P. Chen, J.-X. Jiang and Y. Chen, *Adv. Energy Mater.*, 2018, **8**, 1801326.
30. H. Liu, J. Li, L. Wang, Y. Tang, B. Y. Xia and Y. Chen, *Nano Res.*, 2017, **10**, 3324-3332.
31. H. Yang, Z. Yu, S. Li, Q. Zhang, J. Jin and J. Ma, *J. Catal.*, 2017, **353**, 256-264.
32. Y. Chen, Z. Fan, Z. Luo, X. Liu, Z. Lai, B. Li, Y. Zong, L. Gu and H. Zhang, *Adv. Mater.*, 2017, **29**, 1701331.
33. L. Karuppasamy, S. Anandan, C.-Y. Chen and J. J. Wu, *Electrocatalysis*, 2017, **8**, 430-441.
34. L. Chen, L. Lu, H. Zhu, Y. Chen, Y. Huang, Y. Li and L. Wang, *Nat. Commun.*, 2017, **8**, 14136.
35. Z. Chen, J. Zhang, Y. Zhang, Y. Liu, X. Han, C. Zhong, W. Hu and Y. Deng, *Nano Energy*, 2017, **42**, 353-362.
36. C. Zhu, Q. Shi, S. Fu, J. Song, H. Xia, D. Du and Y. Lin, *Adv. Mater.*, 2016, **28**, 8779-8783.
37. B. Cai, D. Wen, W. Liu, A. K. Herrmann, A. Benad and A. Eychmuller, *Angew. Chem. Int. Ed.*, 2015, **54**, 13101-13105.
38. W. Hong, J. Wang and E. Wang, *ACS Appl. Mater. Interfaces*, 2014, **6**, 9481-9487.
39. C. Wang, P. Song, F. Gao, T. Song, Y. Zhang, C. Chen, L. Li, L. Jin and Y. Du, *J. Colloid Interface Sci.*, 2019, **544**, 284-292.
40. X. Guo, H. Shang, J. Guo, H. Xu and Y. Du, *Appl. Surf. Sci.*, 2019, **481**, 1532-1537.
41. J. Lai, F. Lin, Y. Tang, P. Zhou, Y. Chao, Y. Zhang and S. Guo, *Adv. Energy Mater.*, 2019, **9**.
42. K. Cai, Y. Liao, H. Zhang, J. Liu, Z. Lu, Z. Huang, S. Chen and H. Han, *ACS Appl. Mater. Interfaces*, 2016, **8**, 12792-12797.
43. S. Li, J. Lai, R. Luque and G. Xu, *Energy Environ. Sci.*, 2016, **9**, 3097-3102.
44. W. Hong, C. Shang, J. Wang and E. Wang, *Energy Environ. Sci.*, 2015, **8**, 2910-2915.
45. W. Hong, J. Wang and E. Wang, *Nanoscale*, 2016, **8**, 4927-4932.
46. A. Zalineeva, A. Serov, M. Padilla, U. Martinez, K. Artyushkova, S. Baranton, C. Coutanceau and P. B. Atanassov, *J. Am. Chem. Soc.*, 2014, **136**, 3937-3945.